Electronic Supplementary Material (ESI) for Physical Chemistry Chemical Physics.

Ultrafast charge transfer excited state dynamics in trifluoromethyl-substituted iridium(III) complexes

Electronic supplementary information

Robin Bevernaegie,[a] Lionel Marcélis,[a] Angélica Moreno-Betancourt,[b] Baptiste Laramée-Milette,[c] Garry S. Hanan,[c] Frédérique Loiseau,[b] Michel Sliwa[d] and Benjamin Elias[a]**

a. Université catholique de Louvain (UCL), Institut de la Matière Condensée et des Nanosciences (IMCN), Place Louis Pasteur, 1 box L4.01.02, B-1348 Louvain-la-Neuve, Belgium. E-mail: benjamin.elias@uclouvain.be

b. Département de Chimie Moléculaire, Université Grenoble-Alpes, CNRS UMR 5250, BP53 38041 Grenoble, France.

c. Département de Chimie, Pavillon J.-A. Bombardier, 5155 Chemin de la Rampe, Université de Montréal, Montréal, Québec, Canada, H3T 2B1.

d. Université de Lille, CNRS, UMR 8516, LASIR, Laboratoire de Spectrochimie Infrarouge et Raman, F59000 Lille, France. E-mail: michel.sliwa@univ-lille1.fr

Electronic supplementary information

Table of contents

Experimental details

Steady-state spectroscopy

UV/Vis absorption spectra were recorded on a Shimadzu UV-1700. Room temperature fluorescence spectra were recorded on a Varian Cary Eclipse instrument.

Ultrafast transient absorption

The ultrafast transient absorption experiments were carried out using a set up described elsewhere[1]. Briefly, a 1-kHz Ti:sapphire laser system delivered 100 fs (1.1 mJ) pulses at 800 nm. The 380 nm excitation pulses were obtained through an OPA and at the sample the energy was about 2 µJ / pulse at the sample position with a spot diameter of about 0.4 mm (FWHM). The white light continuum probe beam was generated by focusing the fundamental beam in a 2-mm CaF2 rotating plate. The pump-probe polarization configuration was set at the magic angle (54.7°) and the probe pulse was delayed in time relative to the pump pulse using an optical delay line. The white-light continuum was split into a probe beam (with pump) and a reference beam (without pump). The transmitted light of the probe and the reference beam was recorded on two different channels of a multichannel spectrograph equipped with a CCD camera (Princeton Instrument) and the transient spectra were computed. Each time delay spectrum is the average of 1200 pulses. The solution of IR complexes (absorbance ca. 0.8 at 380 nm, 1 mm) was inside a flow cell (1 mm thick CaF2 windows, optical path length 1 mm). pump beam). The instrument response function (110 fs FWHM) was estimated using the stimulated Raman amplification signal in solvent. All experimental data were corrected by the group velocity dispersion and a global decay analysis (using Igor Pro 6.20) was applied to determine time constants for the transients. Decay associated spectra were obtained by global fitting with three exponential functions and a constant convoluted with a Gaussian pulse of 110 fs (FWHM).

Nanosecond transient absorption

Transient absorption spectra were acquired using a LP920K system from Edinburgh Instruments. Excitation was carried out from the third-harmonic (355 nm) of a Brillant-Quantel Nd:YAG laser at 6 Hz. A Xe900 pulsed Xenon Lamp was used as probe source. The photons were dispersed using a monochromator, transcripted by a R928 (Hamamatsu) photomultiplicator and recorded on a TDS3012C (Tectronix) oscilloscope.

Single Photon Counting

Luminescence lifetimes measurements were performed after irradiation at λ = 400 nm obtained by the second harmonic of a Titanium:Sapphire laser (picosecond Tsunami laser spectra physics 3950-M1BB+39868-03 pulse picker doubler) at a 80 kHz repetition rate. Fluotime 200 from AMS technologies was used for the decay acquisition. It consists of a GaAs microchannel plate photomultiplier tube (Hamamatsu model R3809U-50) followed by a time-correlated single photon counting system from Picoquant (PicoHarp300). Luminescence decays were analyzed with FLUOFIT software available from Picoquant.

Electrochemistry

Cyclic voltammetry was carried out in a one-compartment cell, using a glassy carbon disk working electrode (approximate area = 0.03 cm^2), a platinum wire counter electrode and an Ag/AgCl reference electrode (salt bridge: 3 mol L^{-1} KCl/saturated AgCl). The potential of the working electrode was controlled by an Autolab PGSTAT 100 potentiostat through a PC interface. The cyclic voltammograms were recorded with a sweep rate of 100 $mV.s^{-1}$, in dried acetonitrile (Acros, HPLC grade). Tetrabutylammonium perchlorate (0.1 M) was used as supporting electrolyte and the samples were purged with nitrogen before each measurement.

Spectroelectrochemistry

Electrolysis was run under argon in a dryglovebox at room temperature using a Biologic SP300 potentiostat. A standard three-electrode electrochemical cell was used. Potentials were referred to an $Ag/AgNO_3$ 10 mM reference electrode in CH_3CN + 0.1 M $TBAPF_6$. Absorption spectra were recorded using a Zeiss spectrophotometer (MCS 501 UV-NIR).

Computational calculations

All calculations were performed with the Gaussian09[2], revision E.0 suite of programs employing the DFT method, the Becke three-parameter hybrid functional, and Lee-Yang-Parr’s gradient-corrected correlation functional (B3LYP)[3-5]. All elements except iridium were assigned the 6-31G*(d,p) basis set. The double- ζ quality SBKJC VDZ ECP basis set with an effective core potential was employed for the Ir ion[6-9]. No imaginary frequencies were obtained when frequency calculations on optimized geometries were performed. GaussView 5.0.9[10], GaussSum 3.0[11] and Chemissian 4.30[12] software were used for data analysis, visualization and surface plots. All calculations were performed in a MeCN solution by using the polarized continuum solvation model, as implemented in Gaussian 09[13, 14].

Synthetic details

All solvents and reagents for the synthesis were of reagent grade and were used without further purification. All solvents for the spectroscopic and electrochemical measurements were of spectroscopic grade. Water was purified with a Millipore Milli-Q system. ^{1}H NMR and ^{19}F NMR experiments were performed in CD_3CN on a Bruker AC-300 Avance II (300 MHz) or a Bruker AM-500 (500 MHz) at 20 °C. The chemical shifts (given in ppm) were measured versus the residual peak of the solvent as internal standard. High-resolution mass spectrometry (HRMS) was performed with a Q-Extractive orbitrap from ThermoFisher using reserpine as the internal standard. Samples were ionized by Electrospray Ionization (ESI) and the typical source conditions were: capillary temperature 320 °C, vaporizer temperature 320 °C, sheath gas flow rate = 5 mL/min.

General method for complex synthesis

The cyclometalated Ir(III) chloro-bridged dimer $[Ir(\mu\text{-}ppyCF_3)_2Cl]_2$ (40.4 mg, 0.025 mmol, 1 eq.) and the corresponding ligand **L** (0.055 mmol, 2.2 eq.) were suspended in 4 mL ethylene glycol. The mixture was heated for 5h at 150 °C under argon atmosphere in the dark. After being cooled to room temperature, 10 mL saturated aqueous solution of NH_4PF_6 was added. Then, the precipitate was centrifuged, washed successively with water (three times), ethanol and diethyl ether to finally give a yellow-orange powder after drying under vacuum.

Ir-bpy

$[Ir(ppyCF_3)_2bpy]^+.PF_6^-$ was obtained by using the synthetic procedure described above with 2,2'-dipyridyl as ligand **L** (8.6 mg, 0.055 mmol, 2.2 eq.), to give a pale yellow powder (35 mg, 65% yield). **^{1}H NMR** (500 MHz, CD_3CN) δ 8.44 (m, 4H), 8.24 (d, 2H), 8.15 (td, 2H), 7.84 (td, 2H), 7.78 (m, 4H), 7.50 (m, 2H), 7.29 (d, 2H), 6.96 (td, 2H). **^{19}F NMR** (282 MHz, CD_3CN) δ -59.76 (s), -62.97 (s), -72.94 (d, $J_{19F\text{-}31P}$ = 706.4 Hz). **HRMS** (ESI) m/z calculated for $[C_{36}H_{20}N_4F_{12}{}^{193}Ir - PF_6]^+$ = 929.11201; found 929.11095.

Ir-pzpy

$[Ir(ppyCF_3)_2pzpy]^+.PF_6^-$ was obtained by using the synthetic procedure described above with 2-(pyridin-2-yl)pyrazine as ligand **L** (8.6 mg, 0.055 mmol, 2.2 eq.), to give a yellow powder (32.2 mg, 60% yield). **^{1}H NMR** (500 MHz, CD_3CN) δ 9.64 (d, 1H), 8.69 (d, 1H), 8.56 (d, 1H), 8.46 (s, 2H), 8.25 (m, 2H), 8.20 (dt, 1H), 7.89 – 7.84 (m, 2H), 7.80 (m, 3H), 7.74 (dd, 1H), 7.58 (ddd, 1H), 7.32 (d, 1H), 7.27 (d, 1H), 7.01 – 6.94 (m, 2H). **^{19}F NMR** (282 MHz, CD_3CN) δ -59.62 (s), -59.72 (s), -63.00 (s), -72.94 (d, $J_{19F\text{-}31P}$ = 706.4 Hz). **HRMS** (ESI) m/z calculated for $[C_{35}H_{19}N_5F_{12}{}^{193}Ir - PF_6]^+$ = 930.10726; found 930.10658.

Ir-TAP

$[Ir(ppyCF_3)_2TAP]^+.PF_6^-$ was obtained by using the synthetic procedure described above with 1,4,5,8-tetraazaphenanthrene as ligand **L** (10.0 mg, 0.055 mmol, 2.2 eq.), to give an orange powder (34.6 mg, 63% yield). **^{1}H NMR** (500 MHz, CD_3CN) δ 9.21 (d, 2H), 8.57 (s, 2H), 8.52 (s, 2H), 8.24 (d, 2H), 8.10 (d, 2H), 7.87 (s, 2H), 7.78 (ddd, 2H), 7.18 (dd, 2H), 6.75 (ddd, 2H). **^{19}F NMR** (282 MHz, CD_3CN) δ -59.47 (s), -62.99 (s), -72.99 (d, $J_{19F\text{-}31P}$ = 706.2 Hz). **HRMS** (ESI) m/z calculated for $[C_{36}H_{18}N_6F_{12}{}^{191}Ir - PF_6]^+$ = 953.10018; found 953.10020.

Time-resolved spectroscopy data

Ir-bpy

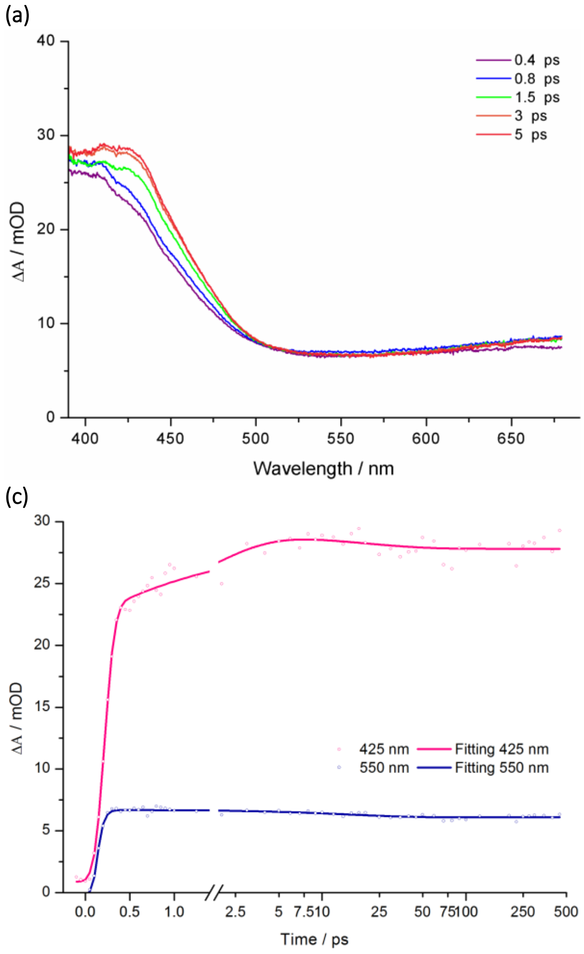

Figure S1. (a) Ultrafast transient absorption spectra (0-5 ps) of **Ir-bpy** in MeCN after excitation at 380 nm. **(b)** Ultrafast transient absorption spectra (5-400 ps) of **Ir-bpy** in MeCN after excitation at 380 nm. **(c)** Transient signals of **Ir-bpy** at 425 (red) and 550 nm (blue) as function of time. The points correspond to experimental data. The lines represent the fitting with a mono-exponential model (550 nm) τ = 16 ps and a double-exponential model (425 nm) τ_1 = 1.2 ps and τ_2 = 16 ps. The long-living component has been fixed by nanosecond transient absorption.

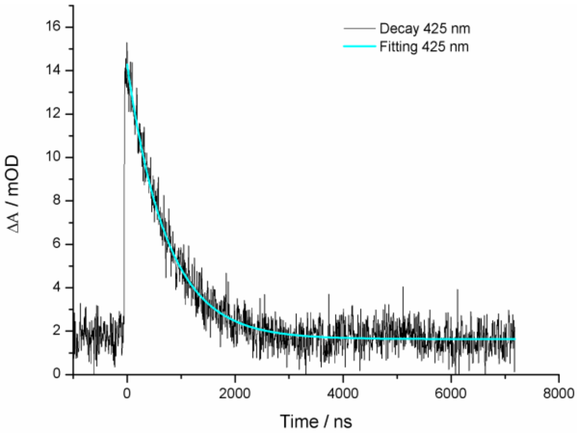

Figure S2. Decay of the signal at 425 nm for **Ir-bpy** obtained by nanosecond transient absorption after excitation at 355 nm; experimental data (dark), fitting (blue) achieved with a mono-exponential model (**$\tau_{long\text{-}living}$ = 730 ± 10 ns**).

Ir-TAP

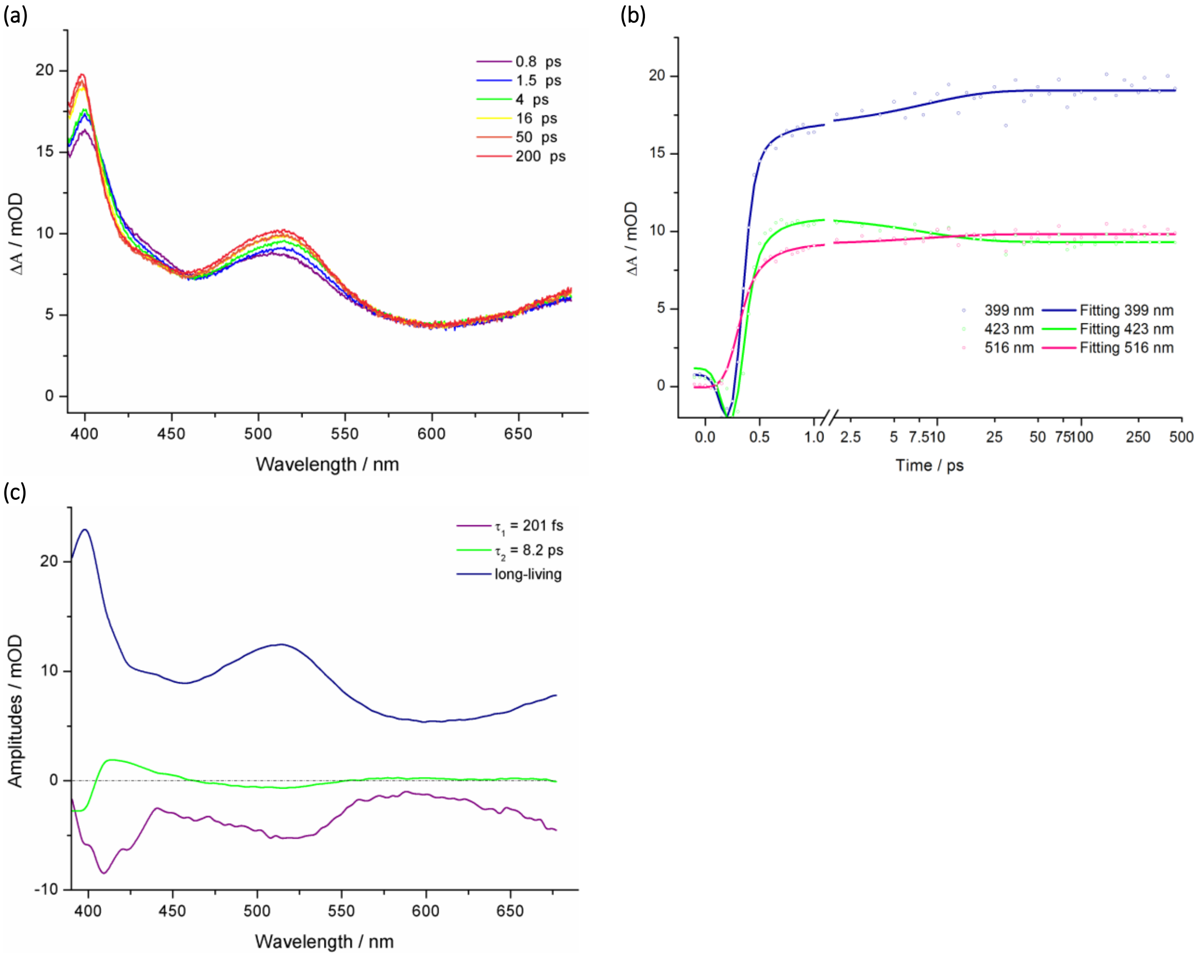

Figure S3. (a) Ultrafast transient absorption spectra of **Ir-TAP** in MeCN after excitation at 380 nm. **(b)** Transient signals of **Ir-bpy** at 399 (blue), 423 (green) and 516 nm (red) as function of time. The points correspond to experimental data. The lines represent the fitting with a double-exponential model τ_1 = 0.2 ps and τ_2 = 8.2 ps. **(c)** Decay associated spectra of **Ir-TAP** obtained with a double-exponential model, τ_1 = 0.2 ps and τ_2 = 8.2 ps. The long-living component has been fixed by nanosecond transient absorption.

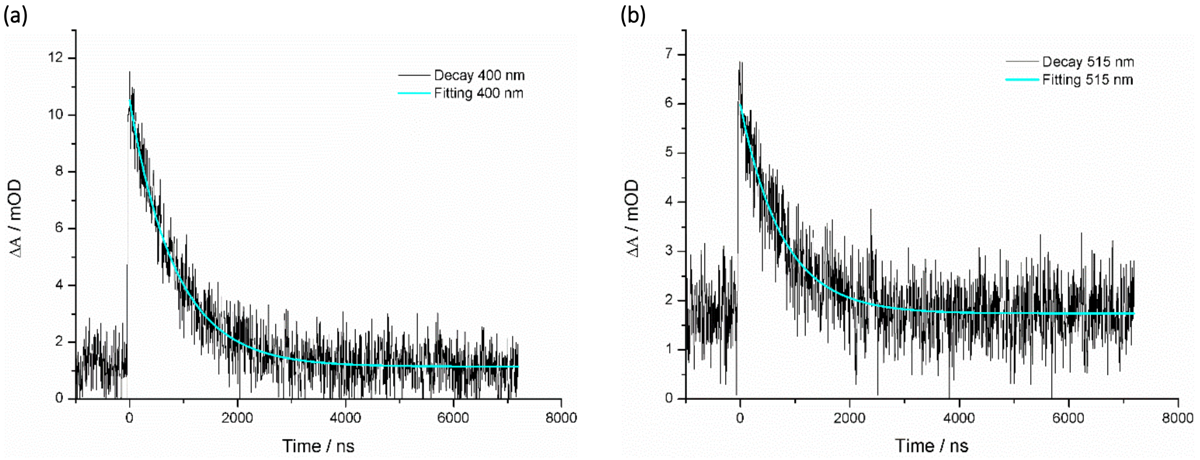

Figure S4. (a) Decay of the signal at 400 nm obtained for **Ir-TAP** by nanosecond transient absorption after excitation at 355 nm; experimental data (dark), fitting (blue) achieved with a mono-exponential model (**$\tau_{long\text{-}living}$ = 848 ± 16 ns**). **(b)** Decay of the signal at 515 nm obtained for **Ir-TAP** by nanosecond transient absorption after excitation at 355 nm; experimental data (dark), fitting (blue) achieved with a mono-exponential model (**$\tau_{long\text{-}living}$ = 770 ± 27 ns**).

Ir-pzpy

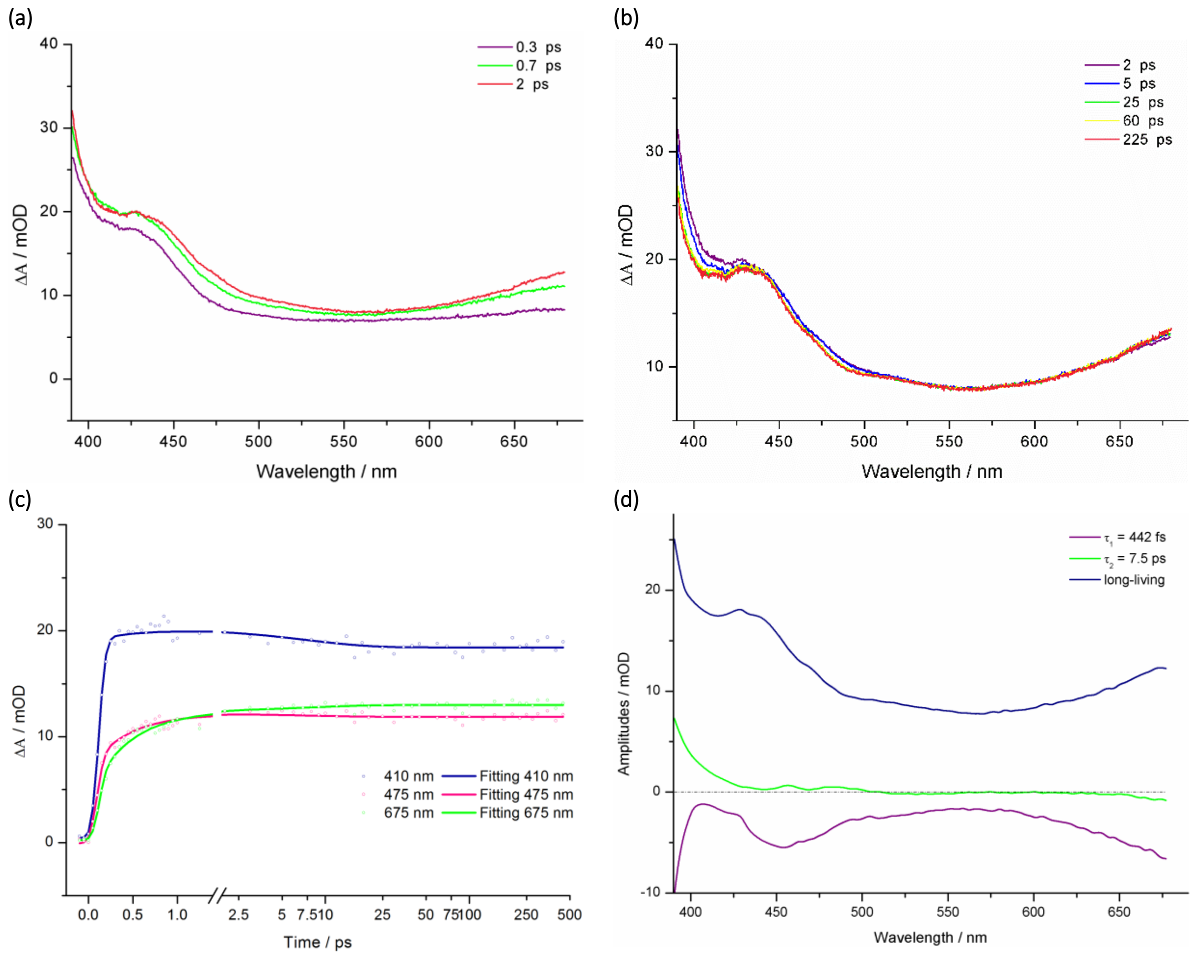

Figure S5. (a) Ultrafast transient absorption spectra (0-2 ps) of **Ir-pzpy** in MeCN after excitation at 380 nm. **(b)** Ultrafast transient absorption spectra (2-225 ps) of **Ir-pzpy** in MeCN after excitation at 380 nm. **(c)** Transient signals of **Ir-pzpy** at 410 (blue), 475 (red) and 675 nm (green) as function of time. The points correspond to experimental data. The lines represent the fitting with a double-exponential model τ_1 = 0.4 ps and τ_2 = 7.5 ps. **(d)** Decay associated spectra of **Ir-pzpy** obtained with a double-exponential model, τ_1 = 0.4 ps and τ_2 = 7.5 ps. The long-living component has been fixed by nanosecond transient absorption.

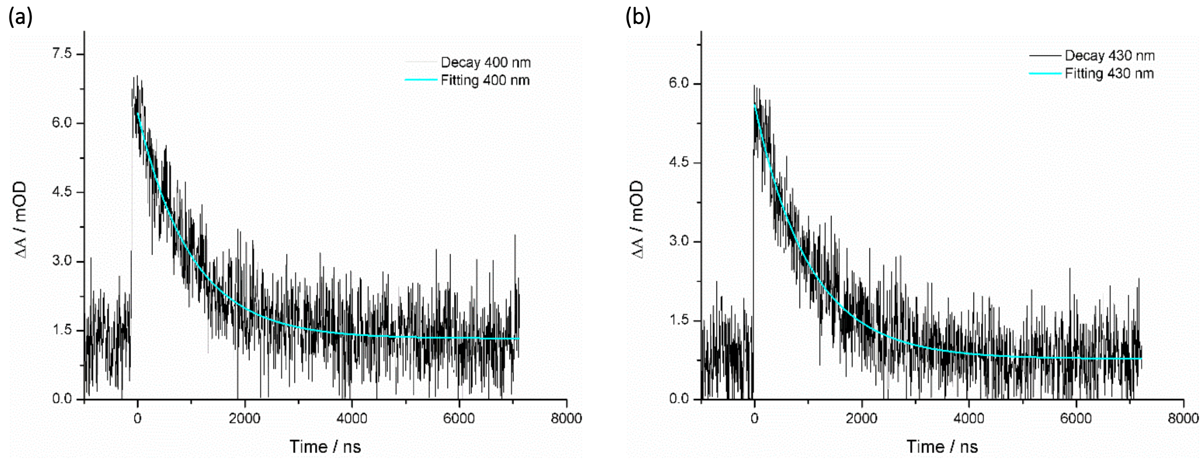

Figure S6. (a) Decay of the signal at 400 nm obtained for **Ir-pzpy** by nanosecond transient absorption after excitation at 355 nm; experimental data (dark), fitting (blue) achieved with a mono-exponential model (**$\tau_{long\text{-}living}$ = 999 ± 31 ns**). **(b)** Decay of the signal at 430 nm obtained for **Ir-pzpy** by nanosecond transient absorption after excitation at 355 nm; experimental data (dark), fitting (blue) achieved with a mono-exponential model (**$\tau_{long\text{-}living}$ = 1026 ± 27 ns**).

Electrochemical and spectroelectrochemical data

Electrochemical data

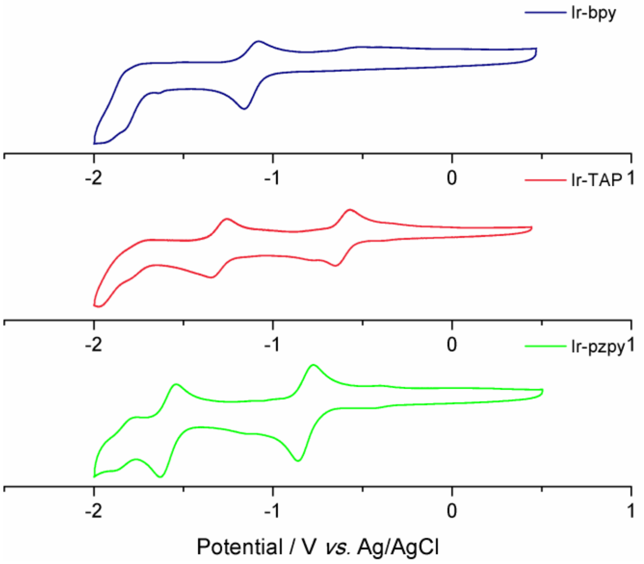

Figure S7. Cyclic voltammograms for the reduction scans of **Ir-bpy** (blue), **Ir-TAP** (red) and **Ir-TAP** (green) in MeCN (0.1 V/s) with Bu_4NClO_4 0.1 M as supporting electrolyte.

Spectroelectrochemical data

Ir-bpy

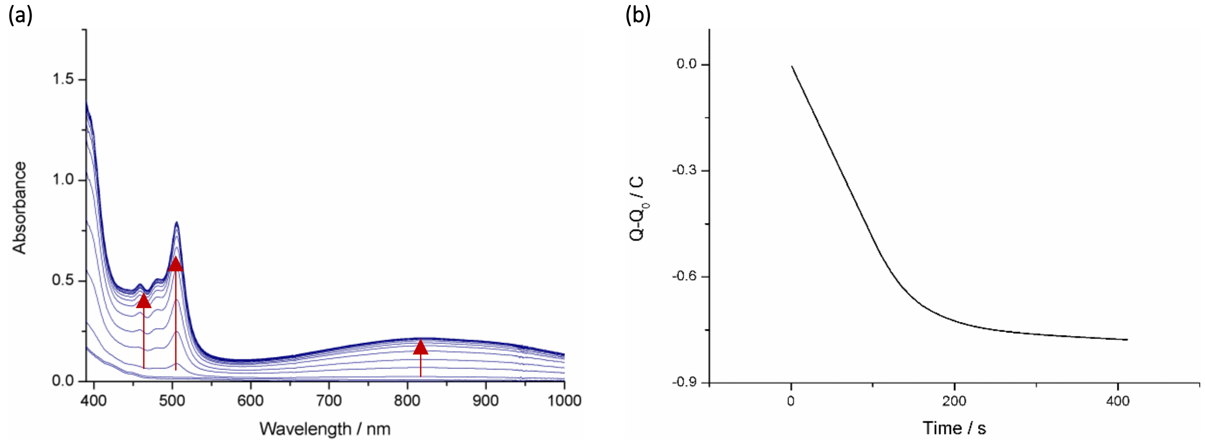

Figure S8. (a) Evolution of the absorption spectrum of **Ir-bpy** during the electrolysis at a potential of -1.8 V *vs.* Ag/$AgNO_3$. **(b)** Evolution of the charge during the electrolysis at a potential of -1.8 V *vs.* Ag/$AgNO_3$ as function of time.

Ir-TAP

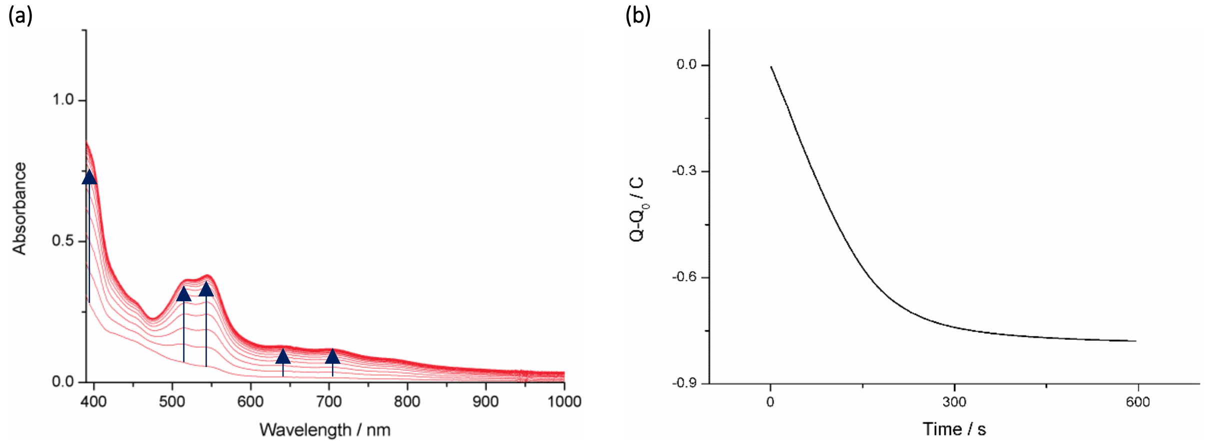

Figure S9. (a) Evolution of the absorption spectrum of **Ir-TAP** during the electrolysis at a potential of -1.2 V *vs.* Ag/AgNO$_3$. **(b)** Evolution of the charge during the electrolysis at a potential of -1.2 V *vs.* Ag/AgNO$_3$ as function of time.

Ir-pzpy

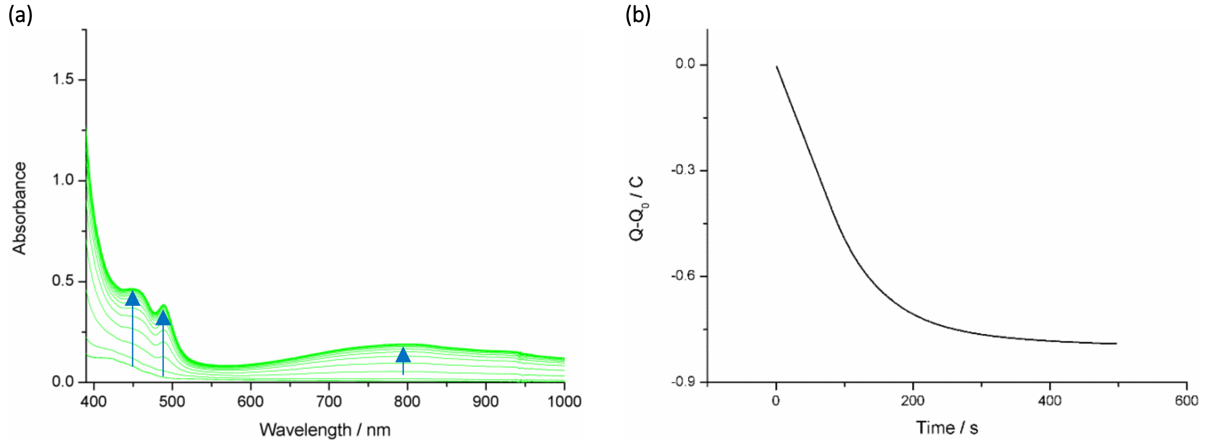

Figure S10. (a) Evolution of the absorption spectrum of **Ir-pzpy** during the electrolysis at a potential of -1.5 V *vs.* Ag/AgNO$_3$. **(b)** Evolution of the charge during the electrolysis at a potential of -1.5 V *vs.* Ag/AgNO$_3$ as function of time.

Computational details

Ir-bpy

Table 1. MO composition of **Ir-bpy** in (*S=0*) ground state with **CPCM: MeCN**.

MO	Energy (eV)	Composition		
		Ir	bpy	ppyCF$_3$
L+5	-1.352	4	20	77
L+4	-1.456	1	94	5
L+3	-1.696	1	72	26
L+2	-1.979	5	7	88
L+1	-2.034	3	3	94
LUMO	**-2.628**	**2**	**97**	**1**
HOMO	**-6.271**	**36**	**2**	**62**
H-1	-6.821	1	0	99
H-2	-6.907	62	7	31
H-3	-6.958	63	8	29
H-4	-7.148	17	5	79
H-5	-7.446	3	95	3
H-6	-7.494	7	1	92

Table 2. Selected triplet transitions from TD-DFT calculations of **Ir-bpy** in the singlet ground state (PBE0, LANL2DZ, CPCM: MeCN).

Excited state	λ (nm)	Energy (eV)	Major Transitions
T_1	427	2.89	H-1→L+1 (14%) HOMO→LUMO (46%) HOMO→L+2 (18%)
T_2	426	2.90	H-1→L+2 (26%) HOMO→L+1(47%)
T_3	423	2.92	H-1→L+1 (13%) HOMO→LUMO (35%) HOMO→L+2 (15%)
T_4	411	3.00	H-5→LUMO (46%) H-3→LUMO (19%) HOMO→LUMO (15%)
T_5	371	3.33	H-2→LUMO (86%)
T_6	354	3.49	H-5→LUMO (24%) H-3→LUMO (46%)
T_7	353	3.50	H-3→L+1 (12%) H-2→L+2 (11%) HOMO→L+1 (31%)
T_8	351	3.52	H-3→LUMO (19%) H-2→L+1 (11%) HOMO→L+2 (16%)
T_9	341	3.62	H-1→LUMO (91%)
T_{10}	340	3.63	HOMO→L+2 (24%) HOMO→L+3 (16%) HOMO→L+5 (16%)

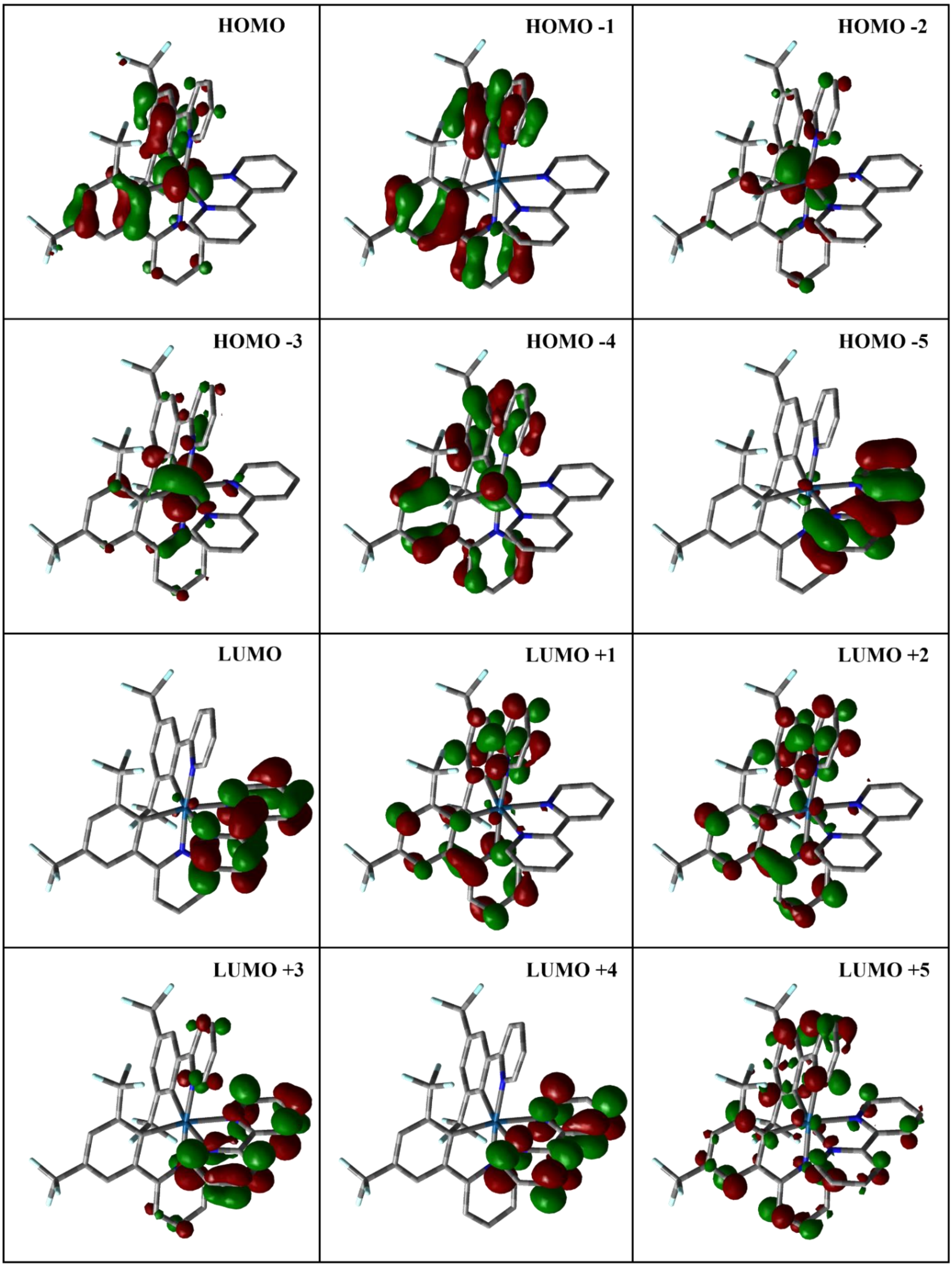

Figure S 11. Kohn-Sham electron density illustration of the molecular orbitals for **Ir-bpy** in (S = 0) ground state with CPCM: MeCN.

Ir-TAP

Table 3. MO composition of **Ir-TAP** in (*S=0*) ground state with **CPCM: MeCN**.

MO	Energy (eV)	Composition		
		Ir	TAP	ppyCF$_3$
L+5	-1.410	4	33	63
L+4	-1.655	1	63	36
L+3	-2.054	5	3	92
L+2	-2.105	2	2	96
L+1	-3.051	1	98	1
LUMO	**-3.223**	**3**	**96**	**1**
HOMO	**-6.390**	**33**	**1**	**66**
H-1	-6.902	0	1	99
H-2	-7.093	56	7	37
H-3	-7.153	35	4	62
H-4	-7.289	46	4	49
H-5	-7.580	8	10	82
H-6	-7.745	3	86	10

Table 4. Selected triplet transitions from TD-DFT calculations of **Ir-TAP** in the singlet ground state (PBE0, LANL2DZ, CPCM: MeCN).

Excited state	λ (nm)	Energy (eV)	Major Transitions
T_1	506	2.44	HOMO→LUMO (97%)
T_2	458	2.69	HOMO→L+1 (94%)
T_3	455	2.71	H-6→L+1 (44%) H-2→L+1 (11%)
T_4	425	2.90	H-2→LUMO (60%) HOMO→L+2 (10%)
T_5	425	2.90	H-1→L+2 (27%) HOMO→L+3 (45%)
T_6	423	2.92	H-1→L+2 (27%) HOMO→L+3 (45%)
T_7	405	3.05	H-2→LUMO (22%) H-1→L+3 (19%) HOMO→L+2 (33%)
T_8	399	3.10	H-6→L+1 (15%) H-4→LUMO (21%) H-3→LUMO (43%)
T_9	389	3.17	H-1→LUMO (84%)
T_{10}	388	3.18	H-9→LUMO (14%) H-8→L+1 (18%) H-7→LUMO (33%) H-2→L+1 (16%)

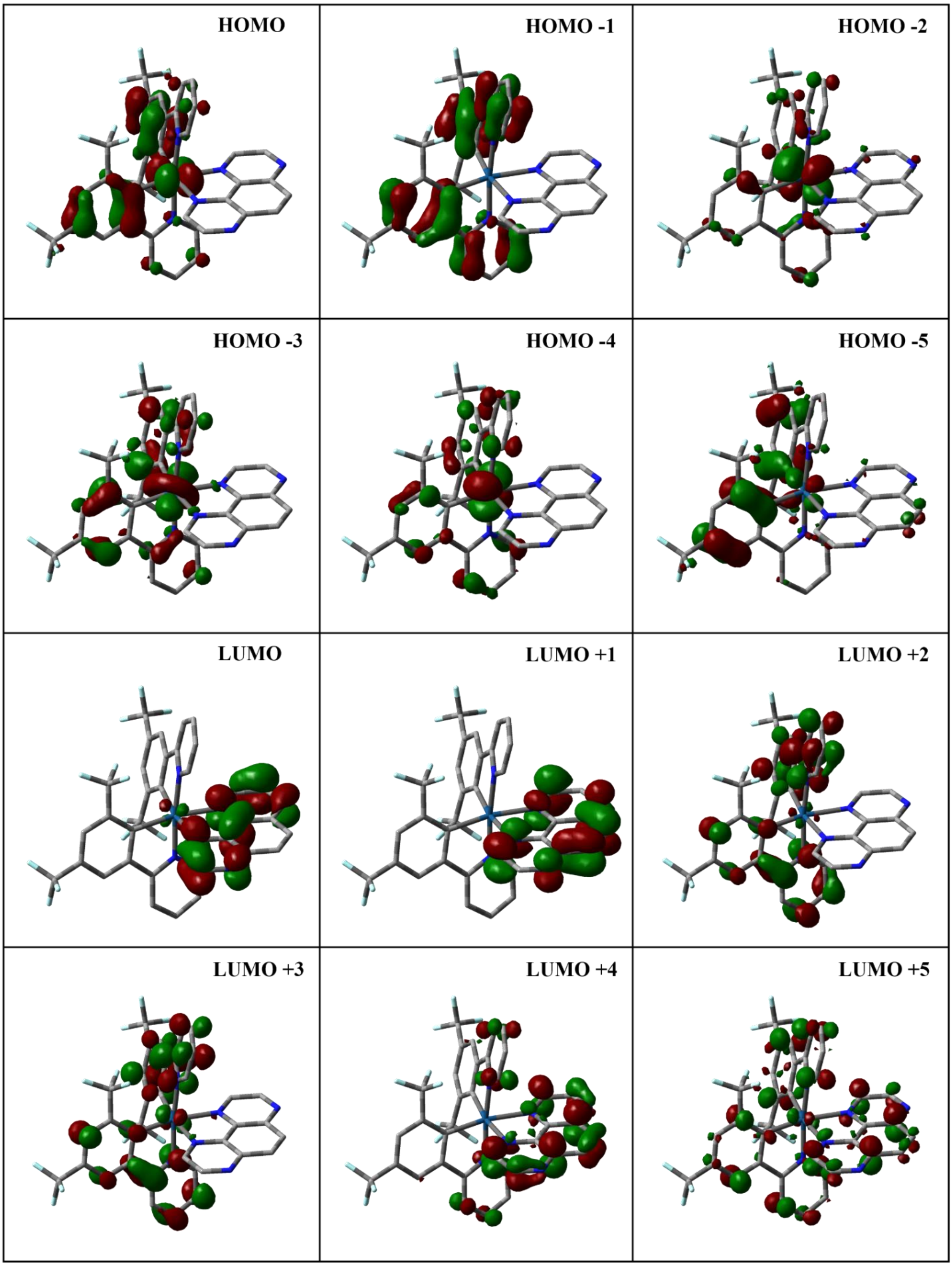

Figure S12. Kohn-Sham electron density illustration of the molecular orbitals for **Ir-TAP** in (S = 0) ground state with CPCM: MeCN.

Ir-pzpy

Table 5. MO composition of **Ir-pzpy** in (*S=0*) ground state with **CPCM: MeCN**.

MO	Energy (eV)	Composition		
		Ir	pzpy	ppyCF$_3$
L+5	-1.416	4	14	82
L+4	-1.671	1	84	15
L+3	-1.975	3	21	76
L+2	-2.065	3	13	84
L+1	-2.165	2	67	30
LUMO	**-2.990**	**3**	**97**	**1**
HOMO	**-6.341**	**34**	**2**	**64**
H-1	-6.863	0	0	99
H-2	-7.011	60	7	33
H-3	-7.071	51	6	43
H-4	-7.213	28	4	67
H-5	-7.544	8	2	90
H-6	-7.641	2	96	3

Table 6. Selected triplet transitions from TD-DFT calculations of **Ir-pzpy** in the singlet ground state (PBE0, LANL2DZ, CPCM: MeCN).

Excited state	λ (nm)	Energy (eV)	Major Transitions
T_1	471	2.635	HOMO→LUMO (97%)
T_2	429	2.888	H-6→LUMO (46%) H-4→LUMO (13%) H-3→LUMO (21%)
T_3	425	2.916	H-1→L+3 (16%) HOMO→L+1 (14%) HOMO→L+2 (30%)
T_4	424	2.923	H-1→L+2 (19%) HOMO→L+2 (12%) HOMO→L+3 (26%)
T_5	400	3.101	H-2→LUMO (81%)
T_6	381	3.239	H-7→LUMO (10%) H-6→LUMO (28%) H-3→LUMO (42%) H-2→LUMO (10%)
T_7	374	3.305	H-1→LUMO (94%)
T_8	363	3.397	H-7→LUMO (59%)
T_9	352	3.505	HOMO→L+1 (40%)
T_{10}	350	3.528	HOMO→L+3 (20%) HOMO→L+5 (11%)

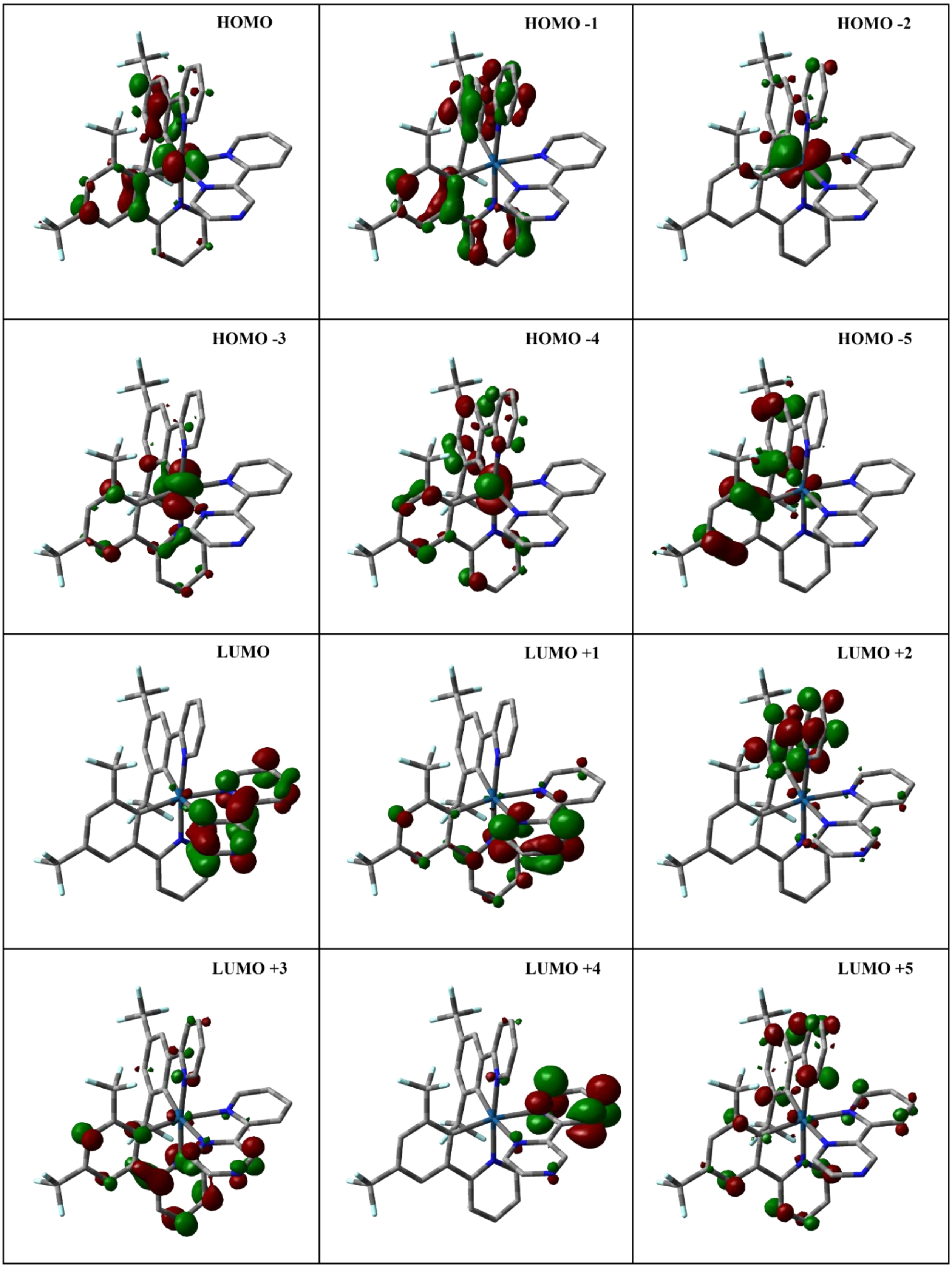

Figure S13. Kohn-Sham electron density illustration of the molecular orbitals for **Ir-pzpy** in (S = 0) ground state with CPCM: MeCN.

References

1. V. Novelli, N. Barbero, C. Barolo, G. Viscardi, M. Sliwa and F. Sauvage, *Phys. Chem. Chem. Phys.*, 2017, **19**, 27670-27681.
2. Frisch, M. J.; Trucks, G. W.; Schlegel, H. B.; Scuseria, G. E.; Robb, M. A.; Cheeseman, J. R.; Scalmani, G.; Barone, V.; Mennucci, B.; Petersson, G. A.; Nakatsuji, H.; Caricato, M.; Li, X.; Hratchian, H. P.; Izmaylov, A. F.; Bloino, J.; Zheng, G.; Sonnenberg, J. L.; Hada, M.; Ehara, M.; Toyota, K.; Fukuda, R.; Hasegawa, J.; Ishida, M.; Nakajima, T.; Honda, Y.; Kitao, O.; Nakai, H.; Vreven, T.; Montgomery, J. A., Jr.; Peralta, J. E.; Ogliaro, F.; Bearpark, M. J.; Heyd, J. J.; Brothers, E. N.; Kudin, K. N.; Staroverov, V. N.; Kobayashi, R.; Normand, J.; Raghavachari, K.; Rendell, A. P.; Burant, J. C.; Iyengar, S. S.; Tomasi, J.; Cossi, M.; Rega, N.; Millam, J. M.; Klene, M.; Knox, J. E.; Cross, J. B.; Bakken, V.; Adamo, C.; Jaramillo, J.; Gomperts, R.; Stratmann, R. E.; Yazyev, O.; Austin, A. J.; Cammi, R.; Pomelli, C.; Ochterski, J. W.; Martin, R. L.; Morokuma, K.; Zakrzewski, V. G.; Voth, G. A.; Salvador, P.; Dannenberg, J. J.; Dapprich, S.; Daniels, A. D.; Farkas, O.; Foresman, J. B.; Ortiz, J. V.; Cioslowski, J.; Fox, D. J. Gaussian 09, revision E.01; Gaussian, Inc.: Wallingford, CT, 2009.
3. B. Miehlich, A. Savin, H. Stoll and H. Preuss, *Chem. Phys. Lett.*, 1989, **157**, 200-206.
4. A. D. Becke, *The Journal of Chemical Physics*, 1993, **98**, 5648-5652.
5. C. Lee, W. Yang and R. G. Parr, *Physical Review B*, 1988, **37**, 785-789.
6. W. J. Stevens, M. Krauss, H. Basch and P. G. Jasien, *Can. J. Chem.*, 1992, **70**, 612-630.
7. T. R. Cundari and W. J. Stevens, *The Journal of Chemical Physics*, 1993, **98**, 5555-5565.
8. W. J. Stevens, H. Basch and M. Krauss, *The Journal of Chemical Physics*, 1984, **81**, 6026-6033.
9. J. S. Binkley, J. A. Pople and W. J. Hehre, *J. Am. Chem. Soc.*, 1980, **102**, 939-947.
10. R. Dennington, J.A. Keith, J.M. Millam GaussView, version 5.0.9; Gaussian Inc.: Shawnee Mission, KS, 2009
11. N. M. O'Boyle, A. L. Tenderholt and K. M. Langner, *J. Comput. Chem.*, 2008, **29**, 839-845.
12. L. Skripnikov, Chemissian, version 4.30; Chemissian, 2005− 2016.
13. S. Miertuš, E. Scrocco and J. Tomasi, *Chem. Phys.*, 1981, **55**, 117-129.
14. J. Tomasi, B. Mennucci and R. Cammi, *Chem. Rev.*, 2005, **105**, 2999-3094.